ACS APPLIED NANO MATERIALS

www.acsanm.org

Article

Open Access

This article is licensed under CC-BY 4.0

1D ZnO Nanostructures in Analytical Systems for Cu(II) and Fe(III) Ion Sensing

Iryna Tepliakova, Mahmoud Abid, Roman Viter,* Simas Rackauskas, Mikhael Bechelany, and Arunas Ramanavicius*

Cite This: *ACS Appl. Nano Mater.* 2026, 9, 3664−3678

Read Online

ACCESS | Metrics & More | Article Recommendations | Supporting Information

ABSTRACT: Heavy metal ion contamination requires sensitive and selective detection methods for environmental and health monitoring. This study demonstrates that one-dimensional (1D) zinc oxide (ZnO) nanostructures with a controlled morphology enable highly sensitive photoluminescence-based detection of Cu^{2+} and Fe^{3+} ions. Three distinct ZnO morphologies—nanotetrapods, nanorods, and nanofibers—were synthesized and comprehensively characterized. ZnO nanotetrapods exhibited promising sensing performance, with detection limits of 0.92 μM for Cu^{2+} and 1.4 μM for Fe^{3+}, response times of 10.6−10.9 ± 2 min, and adequate selectivity over 12 interfering metal cations. The enhanced performance correlates with nanotetrapods' structure properties, defect chemistry, and highly negative surface charge (−42.3 mV at pH 7). We propose a sensing mechanism based on electrostatic ion adsorption followed by charge transfer that reduces Cu^{2+} to Cu^{+} and Fe^{3+} to Fe^{2+} on the ZnO surface, causing photoluminescence quenching. These findings establish the structure−property relationships for ZnO-based sensors with detection capabilities well below the WHO drinking water guidelines, demonstrating their strong potential for environmental monitoring applications.

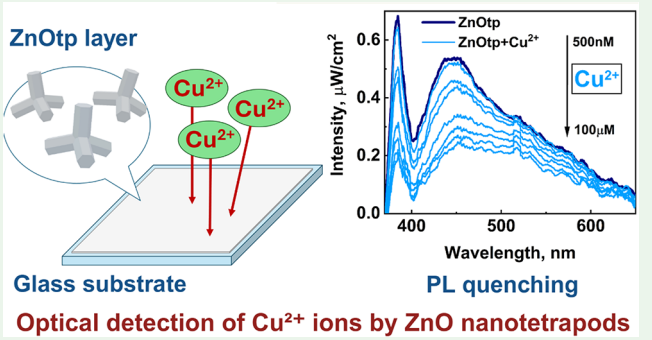

KEYWORDS: *1D ZnO nanostructures, metal ion detection, charge transfer, PL chemical sensors, photocatalytic reduction*

Downloaded via 88.222.25.29 on March 12, 2026 at 14:02:03 (UTC).
See https://pubs.acs.org/sharingguidelines for options on how to legitimately share published articles.

1. INTRODUCTION

Optical chemical sensors are a developing class of analytical methods based on the interaction between target analytes and the sensor surface, converted into changes in optical signals (reflectance, absorbance, photoluminescence, etc.). Photoluminescence (PL) chemical sensors require nanomaterials with chemical stability, high surface-to-volume ratios, and stable PL at room temperature.

Among the various organic and inorganic luminophores, ZnO nanostructures have shown excellent prospects for optical and chemical sensor applications. Zinc oxide (ZnO), a direct-band gap semiconductor, exhibits room-temperature PL across the UV and visible spectrum.[1,2] The tunable electronic and optical properties of ZnO have enabled its application in sensing, catalysis, photocatalysis, photodetectors, and drug delivery.[3−6] ZnO-based optical biosensors and gas sensors have been successfully demonstrated for the detection of biomolecules,[7,8] ochratoxins and aflatoxins,[8] leukemia virus particles,[8,9] and toxic gas compounds.[10,11]

ZnO nanostructures are widely used as adsorbents and photocatalysts.[3,5] The interactions between adsorbates or target molecules and the ZnO surface involve two main mechanisms: electrostatic interactions and degradation caused by reactive oxygen species. The applications of ZnO nanostructures for PL chemical sensors have been partially studied compared with optical biosensor applications. For instance, ZnO nanostructures showed significant photocatalytic and optical sensor performance for the detection of picric acid,[12,13] p-nitrophenol,[14] and ascorbic acid.[15]

Metal ion detection represents an important environmental and health monitoring challenge, as metal ions are present in biological substances (plants and soil), cellular activities, and drinking water. The detection of metal ion concentrations is critical for health and environmental risk assessment. Optical sensors for metal ion detection are particularly promising, as they can overcome the limitations of resistive and electrochemical sensors for measurements in aqueous environments and remote-sensing applications.

The sensor applications of ZnO nanostructures toward metal ions have been partially studied, mainly focusing on electrochemical detection methods. However, despite the role of

Received: November 11, 2025
Revised: January 14, 2026
Accepted: January 16, 2026
Published: February 17, 2026

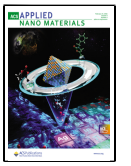

ACS Publications

© 2026 The Authors. Published by American Chemical Society

surface morphology (nanoparticles, nanorods, etc.) and defect concentration in electrochemical sensors having been well explained, the role of optically active defects (zinc interstitials, oxygen vacancies, etc.) in optical chemical sensor applications has not yet been revealed. Several studies have explored the use of ZnO nanostructures for PL-based metal ion sensing. ZnO quantum dots (QDs) have been exploited for optical chemical sensors using PL spectroscopy as the detection method.[16] Dispersed in aqueous solutions, ZnO QDs showed good sensitivity to organic compounds and metal ions, particularly Cr^{3+},[17] Cu^{2+},[16] and Cd^{2+} cations.[18] The detection mechanism of these ZnO sensors was explained by the interaction between surface defects (O/Zn vacancies, O/Zn interstitials) and target analytes.[16−18] For instance, ZnO nanostructures in suspension exhibited high sensitivity toward Cu^{2+} ions within the concentration range of 1−200 μM.[19] Surface modification of ZnO properties enabled the detection of Cu^{2+}, Cr^{6+}, and Fe^{3+} at concentration ranges of 0−1 μM, 0−0.1 μM, and 0−0.1 μM, respectively.[20] To improve sensitivity and selectivity toward metal ions, ZnO surfaces have been modified by functional groups, with proposed interaction mechanisms between ZnO sensors and metal ions involving $-NH_2$ and −COOH groups.[19,20] A major limitation of ZnO QD applications is QD aggregation and optical signal instability in colloidal suspensions.[16,21] The reported results showed that measurements in suspensions require transfer to solid-state substrates for practical applications. Furthermore, the selectivity of ZnO toward different ions and the cross-sensitivity between the tested ions have not been adequately explained.[19,20] Although changes in the ZnO surface properties have been identified as key factors for sensitivity and selectivity, the sensitivity mechanisms have not been revealed in detail.

As surface properties of ZnO nanostructures define their sensor properties, the concentration of surface defects, depletion layer width, ζ-potential, and functional surface groups are reported as the main parameters defining the response of optical ZnO gas sensors and optical ZnO biosensors.[8−10]

However, despite advances in gas and biosensor measurements, no detailed sensor mechanisms have been proposed for ZnO optical chemical sensors. The relationship among nanostructure morphology, defect chemistry (particularly optically active defects), surface charge, and sensing mechanisms has not been investigated. The role of specific optically active defects in PL chemical sensing remains unexplored. Among the different ZnO nanostructures, one-dimensional (1D) ZnO nanostructures have a high potential for application in optical chemical sensors. Previously, we demonstrated that 1D ZnO nanostructures with a high surface-to-volume aspect ratio, deposited on a glass template, showed stable PL signals.[8]

1D ZnO nanostructures can be fabricated by a number of low-cost fabrication methods with high production yields. Among the different synthesis approaches, gas oxidation methods enable the fabrication of 1D nanostructures with varied morphologies based on the oxidation of Zn particles in high-temperature oxygen flames.[2,22] Our previous work demonstrated that variation of technological parameters enables the control of the final product morphology, from 1D ZnO nanorods to ZnO tetrapods.[23−25] Alternatively, 1D ZnO nanostructures could be obtained by the fabrication of ZnO nanolayers with thickness ranging from 0.5−100 nm on electrospun nanofibers by atomic layer deposition (ALD).[26]

The structure and optical properties of 1D ZnO nanostructures fabricated by gas oxidation and ALD methods have been characterized by X-ray diffraction (XRD), Scanning Electron Microscopy (SEM)/Energy-Dispersive X-ray Spectroscopy (EDX), Transmission electron microscopy (TEM), and X-ray photoelectron spectroscopy (XPS),[8,23−28] revealing stoichiometric ZnO with different defect concentrations. Optical characterization showed that these samples are highly reflective in the visible range and exhibit characteristic absorption bands in the range of 340−390 nm, with band gap values of 3.24−3.26 ± 0.16 eV for tetrapods, nanorods, and nanofibers. The PL properties of 1D ZnO nanostructures showed two main emission peaks located at 380 and 520 nm, with the intensity and peak position varying with excitation power, diameter, length, and crystallinity. The successful application of the developed 1D ZnO nanostructures in optical gas sensors and optical biosensors[8,10] makes them suitable for chemical optical sensor applications.

In this study, we report the sensor properties of 1D ZnO optical chemical sensors toward metal ions. To analyze the interaction between the ZnO surface and target ions, three different types of one-dimensional (1D) ZnO nanostructures (zinc oxide nanotetrapods, ZnOtp; nanorods, ZnOnr; and nanofibers, ZnOnf), deposited on solid substrates, have been tested in a fluidic system. The effects of measurement media (air and methanol) on ZnO optical properties, sensitivity, selectivity, and limit of detection (LOD) toward Cu^{2+} and Fe^{3+} metal ions by 1D ZnO chemical sensors have been investigated. The observed sensor properties of 1D ZnO nanostructures have been discussed. The effects of surface charge, depletion layer width, and types of structural defects in 1D ZnO nanostructures on their sensor properties have been revealed. The mechanisms of interactions between the ZnO surface and metal cations have been proposed. The novel findings of the present work have a significant impact on future trends in ZnO optical chemical sensors.

2. EXPERIMENTAL SECTION

2.1. Chemicals Used for the Investigation

Polyacrylonitrile (PAN) (Mw =150,000), dimethylformamide (ACS reagent, 99.8%), and diethyl zinc (DEZ), ($Zn(CH_2CH_3)_2$) (95% purity, CAS: 557-20-0), and micron-sized Zn particles were purchased (purum-grade, CAS:7440-66-6) from Sigma-Aldrich, $CuCl_2 \times 2H_2O$ (ACS reagent, ≥99.0% purity, CAS: 10125-13-0), $FeCl_3 \times 6H_2O$ (reagent grade, ≥98% p.a., CAS: 10025-77-1), $MnCl_2 \times 4H_2O$ (analytical reagent, ≥99%, p.a., CAS No. 13446-34-9), $MgCl_2 \times 6H_2O$ (reagent grade, ≥98% p.a., CAS No. 7791-18-6), $NiCl_2 \times 6H_2O$ (reagent grade, ≥98% p.a., CAS No. 7791-20-0), $AlCl_3$ (≥99% p.a., anhydrous, sublimated, CAS No. 7446-70-0), LiCl (ACS reagent, ≥99% p.a., CAS: 7447-41-8), $CoCl_2 \times 6H_2O$ (≥99%, p.a., ACS reagent, CAS: 7791-13-1), $CrCl_3 \times 6H_2O$ (≥97%, p.a., CAS: 10060-12-5), $ZnCl_2$ (≥97% p.a., CAS: 7646-85-7), and $CdCl_2 \times 2H_2O$ (ACS reagent, 79.5−81.0%, CAS: 7790-78-5), $Pb(NO_3)_2$ (ACS reagent, ≥99.0% p.a., CAS: 10099-74-8), which were used for the probes preparation, were purchased from Sigma-Aldrich. Ethanol (≥96% purity, denatured, CAS: 64-17-5) and methanol (ROTIPURAN, ≥99,9% purity, CAS: 67-56-1) were purchased from Karl Roth.

2.2. Synthesis of 1D ZnO Nanostructures

ZnOtp with high crystallinity was synthesized by the vapor-phase combustion oxidation of metallic Zn particles in an air atmosphere, following the route described in refs 23,24. The growth of the tetrapods was controlled by oxidation reactions occurring in the vicinity of the surface of the Zn particles. Micrometer-sized Zn powder (purity ≥ 97%, mean particle size ∼5 μm) was fed to the vertical quartz tube reactor, air was drawn from the lab atmosphere, and the total gas flow was adjusted to ∼2.0 L·min^{-1}, which was monitored with a rotameter. The quartz

https://doi.org/10.1021/acsanm.5c05081
ACS Appl. Nano Mater. 2026, 9, 3664−3678

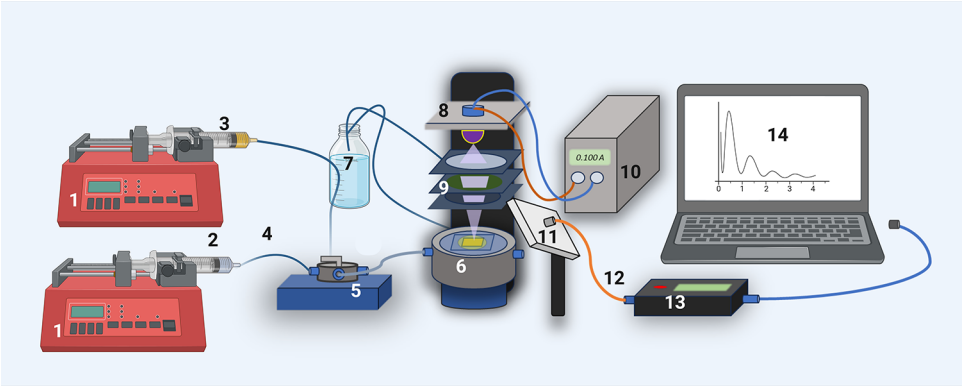

Figure 1. Principal scheme of the fluidic system integrated with PL setup: 1—syringe pumps, 2—syringe with a probe, 3—syringe with liquid for washing, 4—connection tubes, 5—bubbles trap + channel switching valve, 6—chamber with the sample, 7—waist collector, 8—light source, 9—system of lenses and filters, 10—power supply, 11—collimating lens,12—fiber-optic cable, 13—spectrometer, 14—laptop with Ocean Optics software.

tube was heated by a premixed methane−air flame; under these conditions, zinc particles ignited and partially evaporated, forming tetrapodal ZnO via anisotropic vapor−solid growth. ZnOtp formed in the flame region is transported downstream and collected on the nitrocellulose membrane filter (0.4 μm pore size) mounted at the reactor outlet. The residence time of the particles in the hot zone is on the order of a few seconds.

ZnOnr was synthesized by the combustion of micron-sized Zn particles in an air atmosphere. The reaction temperature of 720 °C was maintained in the reactor by using a propane-butane flame at 600 °C. The synthesis procedure and features of the dust burn reactor are detailed in refs 2,22.

ZnOnf structures (ZnO layer thickness of 10 nm) were fabricated by combining atomic layer deposition and electrospun nanofiber membranes. Electrospinning technology was used to fabricate polyacrylonitrile (PAN) fibers on an aluminum substrate, which served as a template for the atomic layer deposition of ZnO to achieve a large active surface area and avoid agglomeration effects. The procedure of synthesis was previously reported in refs 26−28.

ZnOtp and ZnOnr powders were mixed with ethanol (96%) at a concentration of 2 mg/mL and deposited on glass substrates by the "spray dry" method (approximately 0.12−0.15 mg per 1 substrate). The developed samples were dried in an oven at 120 °C for 3 h. Aluminum substrates with ZnOnf were cut into square samples of 0.5 mm × 0.5 mm.

2.3. Investigation of Structural and Optical Properties of the ZnO Nanostructures

The structural properties of the ZnO nanostructures were studied by the X-ray diffraction method using a Bruker D8 Advanced XRD diffractometer equipped with CuKα (Bruker, Billerica).

The size and shape of the fabricated ZnO 1D nanostructures were investigated by scanning electron microscopy (SEM 4800); Hitachi, Tokyo, Japan.

The surface charge of the fabricated ZnO 1D nanostructures was studied by ζ-potential measurements using a Zetasizer Nano ZS instrument (Malvern Instruments Ltd., Malvern, U.K.) and Software Version 7.12 (Malvern Instruments Ltd., Malvern, U.K.).

X-ray photoelectron spectroscopy (ESCALAB 250; Thermofisher Scientific, Waltham, MA) was used for elemental surface analysis. Optical properties were evaluated through reflectance measurements conducted with a Shimadzu 3600 UV−VIS−NIR spectrophotometer (300−800 nm), equipped with an integrating sphere, a slit width of 3 nm, and a wavelength step size of 0.5 nm.

The optical properties were investigated using diffuse reflectance spectroscopy and PL in the wavelength range of 350−800 nm.

Diffuse reflectance was measured using a homemade setup, consisting of a comprehensive band light source from Ocean Optics Ltd. (Orlando), 250−1000 nm, and a fiber-optic spectrometer (Ocean Optics HR4000; Ocean Optics Ltd., Orlando). Diffuse reflectance was recalculated into optical absorbance according to the Kubelka-Munk equation (eq 1)

$$A = \frac{(1-R)^2}{2R},\ 0 < R < 1 \tag{1}$$

where R is the diffuse reflectance value.[8]

The band gap values of the ZnO nanostructures were determined from the optical absorption edge using eq 2

$$(A \times h\nu)^2 = C(h\nu - E_g) \tag{2}$$

where A is the absorption coefficient, $h\nu$ is the incident photon energy, C is a constant, and E_g is the optical band gap.

PL spectroscopy was performed using a fiber-optic spectrometer (Ocean Optics LTD, Orlando), equipped with collimating lenses. The excitation source was a UV LED (325 nm, 15 nm, FWHM, 3 mW output power) by Roitner (Vienna, Austria).

2.4. Investigation of Sensor Properties

The sensitivity and selectivity of the ZnO nanostructures under investigation were examined in a fluidic system using the PL method, according to the principal scheme, as presented in Figure 1. The system for sensor testing was equipped with two syringe pumps for the delivery of metal ion solutions and pure solvent (MeOH) used for washing/regeneration of the system between measurements, a bubble trap membrane, a switch valve, a sample chamber, a 325 nm UV LED, an optical system based on lenses and filters, a fiber-optic light collector, a fiber-optic spectrometer, and a laptop.

The prepared samples were delivered to a sample chamber and excited with a UV light source. The system was filled with methanol at a constant pumping rate of 50 μL/min, ensuring laminar flow and constant pressure. One syringe was filled with pure methanol for washing, and the other syringe contained $CuCl_2 \times 2H_2O$ or $FeCl_3 \times 6H_2O$ solutions in methanol (99,9%). A valve was used to switch the flow from one syringe to the other.

The full PL spectra of the steady-state samples were recorded before and after the addition of each probe. The kinetics of the PL intensity at selected wavelengths were recorded during the adsorption measurements to monitor the real-time changes in the PL intensity induced by metal ion adsorption. After the measurement, the sensor response, limit of detection, time of sensor response, and noise/signal ratio were evaluated.

The sensor response (S) was calculated as follows

$$S = \left|1 - \frac{I(c_n)}{I(c_0)}\right| \tag{3}$$

https://doi.org/10.1021/acsanm.5c05081
ACS Appl. Nano Mater. 2026, 9, 3664−3678

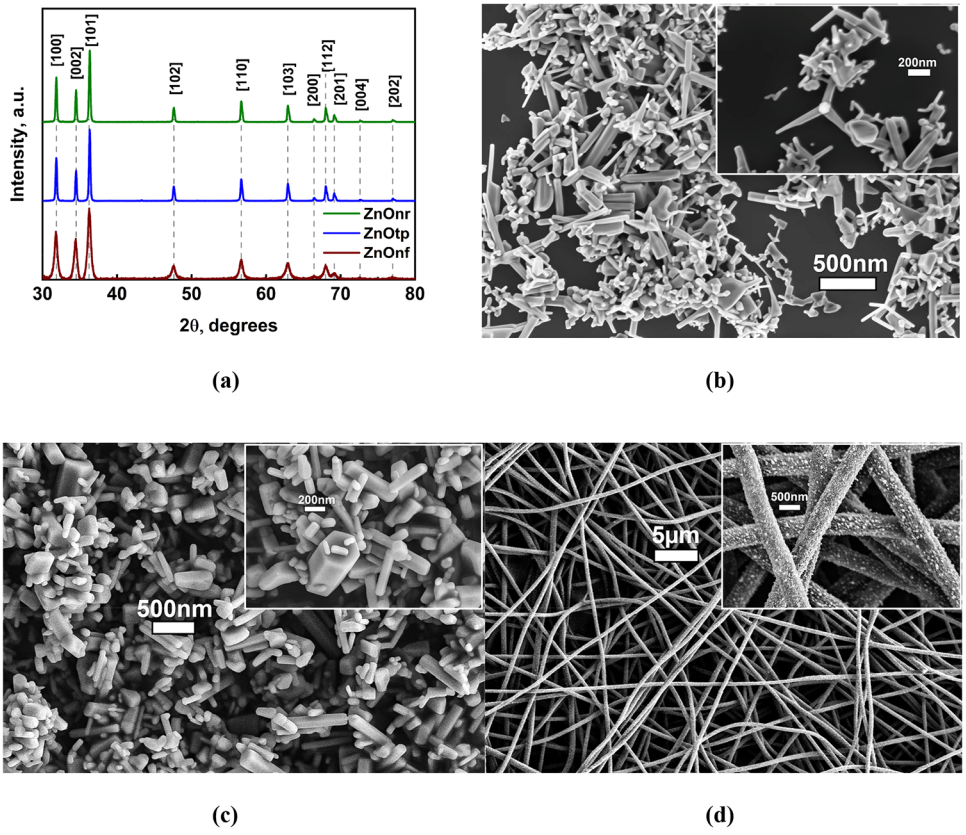

Figure 2. Structural properties of the ZnO-based nanostructures: X-ray spectra of ZnOtp, ZnOnr, ZnOnf (a); SEM images of ZnOtp (b), ZnOnr (c), and ZnOnf (d).

where I (C_0) and I (C_n) are the PL intensities of the pure sample and after adding aliquots containing the corresponding analyte (metal ion) concentration Cn, respectively.[8]

The LOD was calculated by using eq 4

$$\mathrm{LOD} = \frac{3\sigma}{LS} \tag{4}$$

where σ is the standard deviation of the signal, and LS is the linear slope of the sensor response curve.

To assess the interaction mechanisms between the target ions and 1D ZnO nanostructures, XPS measurements of the ZnO nanostructures with adsorbed ions were performed.

Selectivity tests were performed using a fluidic system. The control concentration of the metal salt solutions in MeOH was determined to be 10 μM.

3. RESULTS AND DISCUSSION

3.1. Structure and Optical Properties of 1D ZnO

The XRD patterns of the ZnO nanostructures are shown in Figure 2a. Analysis of the spectra indicates the presence of peaks, which are characteristic of the (100), (002), (101), (102), (110), (103), (200), (112), (004), (104), and (202) planes of zinc oxide (according to JCPDS pattern no: 043-0002). The peak positions of the XRD peaks were identical for all the tested ZnO samples. All three samples showed hexagonal wurtzite-type lattice symmetry. The lattice parameters were determined using the Bragg equation for a hexagonal lattice:

The structural properties of the samples were studied by scanning electron microscopy. Figure 2b−2d shows the SEM images of the investigated ZnO nanostructures. ZnOtp has an average arm length of 334 ± 165 nm and a diameter of 34 ± 16 nm. ZnOnr has an average length of 347 ± 145 nm and a diameter of 41 ± 15 nm. ZnOnf has a length of 2925 ± 865 nm and a diameter of 194 ± 50 nm (the size distribution of lengths and diameters is presented in the Supporting Information, Figure S1).

The specific surface area (SSA) of 1D ZnO nanostructures was evaluated by geometrical modeling using eq S1 for ZnOtp and eq S2 for ZnOnr and ZnOnf (the detailed description is given in the Supporting Materials section). The measured dimensions of the ZnO nanostructures are summarized in Table 1.

Table 1. Linear Dimensions of ZnO Nanostructures

nanostructure	h (nm)	d (nm)	aspect ratio (h/d)
ZnOtp	335 ± 165	33 ± 16	10
ZnOnr	350 ± 145	40 ± 15	8.8
ZnOnf	2923 ± 865	194 ± 50	15.1

The diffuse reflectance of the ZnO nanostructures was investigated in the UV−vis region (300−800 nm) (Figure S12). All samples showed an absorption edge in the range of 350−400 nm, typical of ZnO. Diffuse reflectance of the ZnO nanostructures was recalculated to the optical absorbtion using eq 1 (Figure 3a). The band gap values of the ZnO nanostructures were determined from the optical absorption edge by using eq 2. The calculated values of the band gaps were 3.24 ± 0.16 eV, 3.26 ± 0.16 eV, and 3.25 ± 0.16 eV for ZnOnf, ZnOtp, and ZnOnr, respectively. The calculated values are in good agreement with the results reported in our previous works.[2,22−27]

https://doi.org/10.1021/acsanm.5c05081
ACS Appl. Nano Mater. 2026, 9, 3664−3678

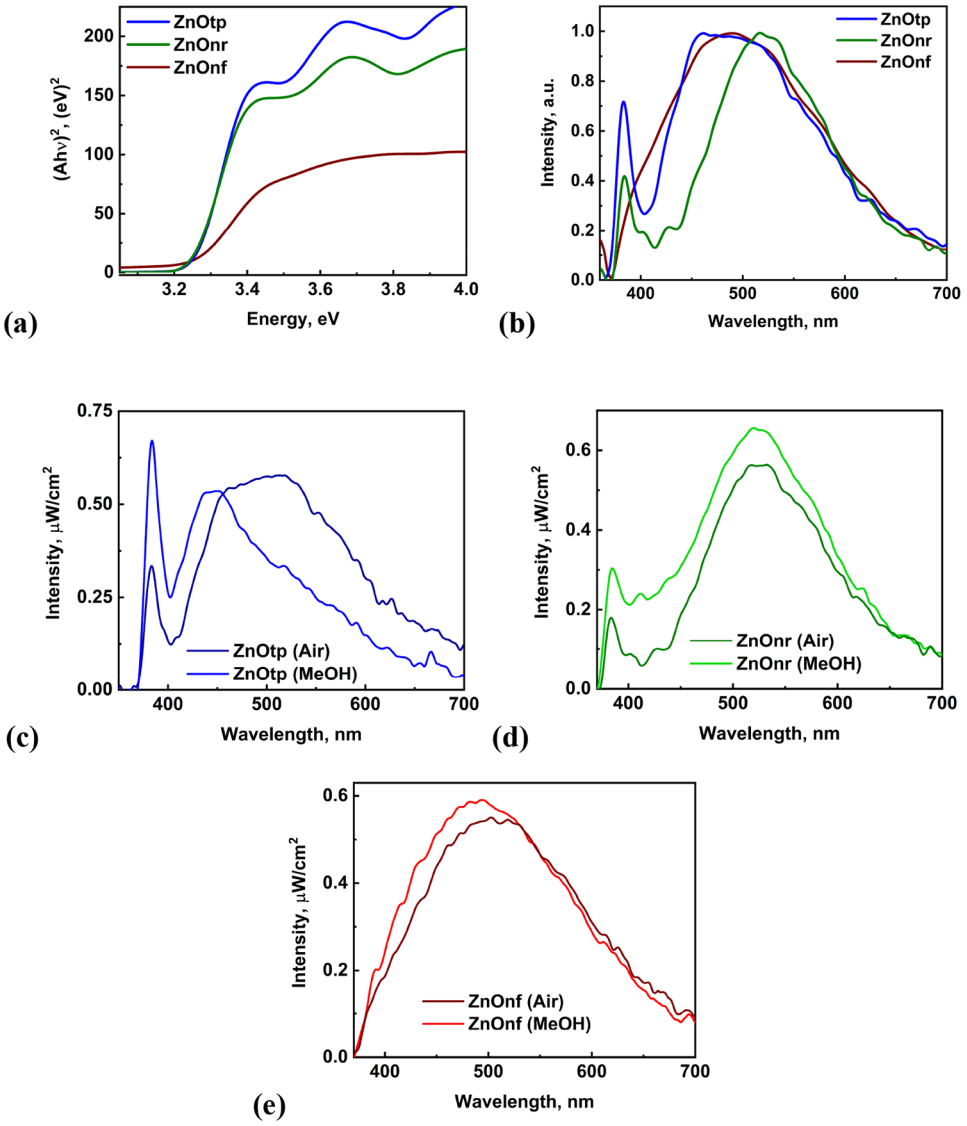

Figure 3. Absorbance (a) and PL (b) spectra of ZnOtp, ZnOnr, and ZnOnf in air. PL spectra of ZnOtp (c), ZnOnr (d), and ZnOnf (e).

Table 2. PL Deconvolution Analysis[29−31]

ZnOtp		ZnOnr		ZnOnf	
no., position of peak's maximum	emission type	no., position of peak's maximum	emission type	no., position of peak's maximum	emission type
I—3.25 eV (381 nm)	free exciton (FX)	I—3.23 eV (384 nm)	FX	I—3.17 eV (391 nm)	V_{Zn}/Zn_i
II—2.92 eV (425 nm)	LO-free exciton phonon replica (FX-LO)	II—3.1 eV (400 nm)	V_{Zn} neutral/Zn_i	II—2.98 eV (416 nm)	V_{Zn}/Zn_i
III—2.92 eV (425 nm)	V_{Zn}/Zn interstitial (Zn_i)	III—2.53 eV (490 nm)	V_O^+	III—2.63 eV (471 nm)	V_O neutral of V_{Zn}^-
IV—2.7 eV (459 nm)	V_{Zn}^-/V[O]	IV—2.31 eV (537 nm)	V_O^{2+}	IV—2.3 eV (539 nm)	V_O^+
V—2.45 eV (506 nm)	V_O^+	V—2.11 eV (588 nm)	O_i/V_{Zn}^{2-}	V—2.1 eV (590 nm)	V_O^{2+}
VI—2.25 eV (551 nm)	V_O^{2+}	VI —1.96 eV (633 nm)	O_i	VI—1.96 eV (633 nm)	O_i
VII—2.1 eV (595 nm)	V_{Zn}^{2-}				
VIII—1.82 eV (683 nm)	interstitial oxygen (O_i)				

The PL spectra of the ZnO nanostructures measured in air are shown in Figure 3b. Two distinct PL emission bands were observed in the spectrum of ZnOtp: in the UV region, centered at 384 nm, attributed to exciton scattering, and in the visible region, centered at 485 nm, associated with intrinsic defects in the ZnO structure. The emission spectrum of ZnOnr exhibited a UV band centered at 384 nm and a visible band centered at 517 nm. ZnOnf showed a wide emission band centered at 500 nm. In order to identify the emission centers, the PL spectra were deconvoluted into elementary emission lines using the Gaussian fitting methodology. The deconvolution results are presented in Figure S2a−c. The peak positions are summarized in Table 2. The full table content and detailed description are provided in Supporting Materials.

https://doi.org/10.1021/acsanm.5c05081
ACS Appl. Nano Mater. 2026, 9, 3664−3678

Previously, we reported on the temperature dependence of the PL of ZnOnf and ZnOnr.[32,33] Based on the peak position and electron−phonon interaction of the ZnO defects, we have shown that the main defect states were oxygen vacancies in ZnOnr and ZnOnf.

In order to identify the emission centers in ZnO nanostructures and distinguish between different types of defects, temperature-dependent PL measurements of ZnOtp were performed (Figure S2d). Based on the temperature measurements of the ZnOtp PL, we observed that new peaks appeared in the range of 400−440 nm at low temperatures and disappeared at higher temperatures.

From the previously published reports, the peaks in the range of 400−440 nm correspond to Zn interstitials.[34−36] It was shown that at room temperature, there is a transition between Zn interstitials and Zn/O vacancies,[35,36] showing blue luminescence (420−440 nm). Changes in the temperature and depletion layer could stimulate transitions between the charged states of defects. In the present work, we could not separate the PL peaks from the neutral oxygen vacancies and Zn interstitials, as the energies of the emitted photons are similar. We can assume that the ZnOtp PL spectrum contains a mixture of neutral oxygen vacancies and Zn interstitials.

In order to understand the mechanisms of luminescence and analyze the optical transitions, we performed a comparative analysis of the ZnO PL in air and methanol (Figure 3c−e). Figure 3c−e shows the change in the PL spectra of 1D ZnO nanostructures in air and methanol. The PL of ZnO increased in methanol. The significant increase and shift of the blue PL peak can be explained by two effects: the change in the depletion layer and the change in emission centers.

The depletion layer width was quantitatively evaluated using the following procedure. In our previous works,[32,33] we proposed calculations of the Debye lengths in ZnOnf and ZnOnr. For ZnOnr, the Debye length was calculated to be about 18 nm. The PL intensity of exciton luminescence I in ZnO is proportional to the depletion layer width W as[37]

$$\ln\left(\frac{1}{I}\right) \sim W \tag{5}$$

The Debye length was calculated by integrating the PL spectra $I(\lambda)$ in the range of 370−400 nm using eq 5. The estimated Debye length for each ZnO sample before and after immersion in methanol is summarized in Table 3:

Table 3. Depletion Layer Width (W) of the 1D ZnO Nanostructures in Air and Methanol

	ZnOtp	ZnOnr	ZnOnf
W, nm (air)	15.3	18	17.9
W, nm (methanol)	12.7	15.3	16.9

Based on the fact that methanol is a hole scavenger and the luminescence intensity of ZnO increased compared to air measurements, we consider that both the depletion layer decrease and hole scavenging on the surface increased the luminescence in the UV−vis ranges.

The fabrication method of ZnO plays an important role in the optical transitions and surface changes. The PL spectra of ZnOtp after immersion in methanol showed a significant change in the visible emission with a peak shift to 437 nm. This effect could be explained by a change in the luminescence states.[38] It was reported that a change in the depletion layer and an increase of charge concentrations could lead to a change in ZnO luminescence due to the transition between the neutral and charged states for one type of defect (like interstitials and vacancies). For instance, ZnOtp showed the highest impact of intensity change and peak shift due to the change in the PL mechanisms.

The PL spectrum of ZnOnr showed only an increase of the intensity, pointing out that electron−acceptor recombination was the dominant mechanism of luminescence. ZnOnf did not show a significant increase of the intensity, which could be explained by an insignificant impact of the methanol hole-scavenging effect on the negative surface charge formed by molecular oxygen.

On the basis of the possible PL optical transitions in ZnO, we assume that the main optical transitions of ZnO in methanol might be between donors and acceptors. It is known that the PL in ZnO in the visible range is explained by the defects of donors (oxygen vacancies, Zn interstitials) and acceptors (Zn vacancies and interstitial oxygen).[31] As photogenerated holes tend to be captured on the surface,[39,40] the main PL channels move to oxygen vacancies and zinc interstitials.[31] Based on the position of the defects in the ZnO band gap, we assume that main transitions might occur between the neutral and single ionized Zn interstitial and zinc vacancies, and between oxygen vacancies and the valence band

The studied interaction between ZnO and methanol vapors showed an increase of the UV peak and a decrease of the visible peak.[41] The increase of the UV peak was explained by the removal of electrons from chemisorbed oxygen species; however, changes in the visible range were not explained. Comparing the measurements in air and methanol in the present work, we can assume that methanol adsorption on the surface of ZnO reduced the depletion layer and changed the PL mechanisms only in ZnOtp.

In order to analyze the charge on the surface of the studied 1D ZnO nanostructures, ζ-potential measurements were performed. The ζ-potential values of the studied ZnO samples, determined at different pH values, are shown in Figure 4. In

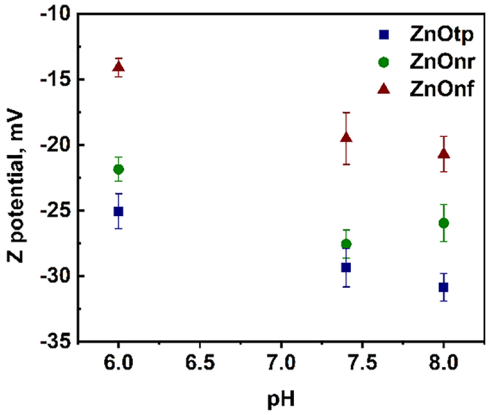

Figure 4. ζ-Potential of the 1D ZnO nanostructures.

accordance with the ζ-potential measurements, the ZnOtp-based surface exhibited the most negative surface charge (Figure 4). The ZnOnr samples exhibited the second-highest negative surface charge, while the nanofiber samples (ZnOnf) demonstrated the lowest absolute charge value.

The ζ-potential measurements are in good correlation with the PL measurements, showing that the negative surface charge,

https://doi.org/10.1021/acsanm.5c05081
ACS Appl. Nano Mater. 2026, 9, 3664−3678

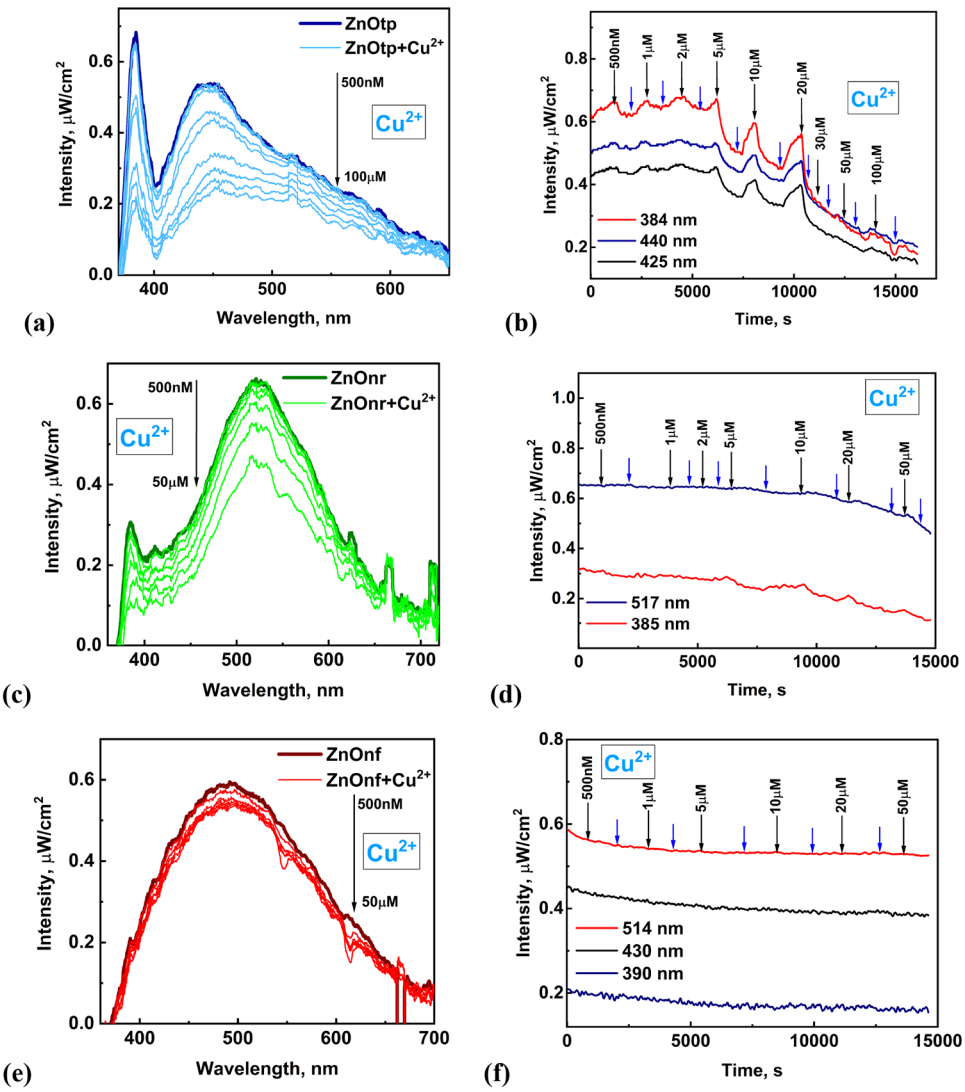

Figure 5. Sensitivity of ZnO structure-based sensors toward Cu^{2+} ions; steady-state PL spectra (a, c, e), and kinetics of the PL (b, d, f) signal (the moment of adding the probe is marked with a black arrow, and the respective concentration is indicated; the moment when the cleaning process started is marked with a blue arrow).

consistent with a high concentration of negatively charged surface defects, could be one of the main factors defining the properties of the ZnO nanostructures.

3.2. Sensitivity of 1D ZnO Nanostructures toward Cu^{2+} and Fe^{3+} ions

Sensor responses of the 1D ZnO nanostructures to Cu^{2+} ions are shown in Figure 5. The intensity of the ZnOtp PL in the UV and visible ranges of the spectra decreased after interaction with Cu^{2+} ions (Figure 5a). The ZnOtp nanostructures did not react with low concentrations of Cu^{2+} ions ($C < 5\ \mu M$) (Figure 5b). A significant response of ZnOtp toward Cu^{2+} ions was observed at concentrations higher than 5 μM. The response time, calculated as 90% of the signal change, was found to be 10.5 $\pm$ 2 min (Figure 5b). From the kinetic measurements (Figure 5b), we found that the adsorption of Cu^{2+} on the surface of ZnOtp was irreversible. Sensors based on ZnOtp nanostructures demonstrated good sensitivity toward Cu^{2+} ions in the range of 5−60 μM.

The intensity of the ZnOnr PL in the UV and visible ranges of the spectra decreased after interaction with Cu^{2+} ions (Figure 5c). The ZnOnr nanostructures did not react with high concentrations of Cu^{2+} ions ($C < 15\ \mu M$) (Figure 5d). A significant response of ZnOnr toward Cu^{2+} ions was observed at concentrations higher than 5 μM. The response time, calculated as 90% of the signal change, was found to be 20 $\pm$ 2 min (Figure 5d). From the kinetic measurements (Figure 5d), we found that the adsorption of Cu^{2+} on the surface of ZnOnr was irreversible. Sensors based on ZnOnr nanostructures demonstrated low sensitivity toward Cu^{2+} ions in the range of 15−60 μM. From Figure 5e,f, we can conclude that ZnOnf did not show any response to Cu^{2+} ions in the range of the tested concentrations

The sensor responses of the 1D ZnO nanostructures to Fe^{3+} ions are shown in Figure 6. Similar to the sensor response of ZnOtp to Cu^{2+} ions, the intensity of the ZnOtp PL in the UV and visible ranges of the spectra decreased after interaction with Fe^{3+} ions (Figure 6a). The ZnOtp nanostructures demonstrated a sensor response to low concentrations of Fe^{3+} ions ($C < 5\ \mu M$) (Figure 6b). The response time, calculated as 90% of the signal change, was found to be 10.9 $\pm$ 2 min (Figure 6b). From the kinetic measurements (Figure 6b), we found that the adsorption of Fe^{3+} on the surface of ZnOtp was partially reversible at low concentrations and irreversible at high concentrations of Fe^{3+}

https://doi.org/10.1021/acsanm.5c05081
ACS Appl. Nano Mater. 2026, 9, 3664−3678

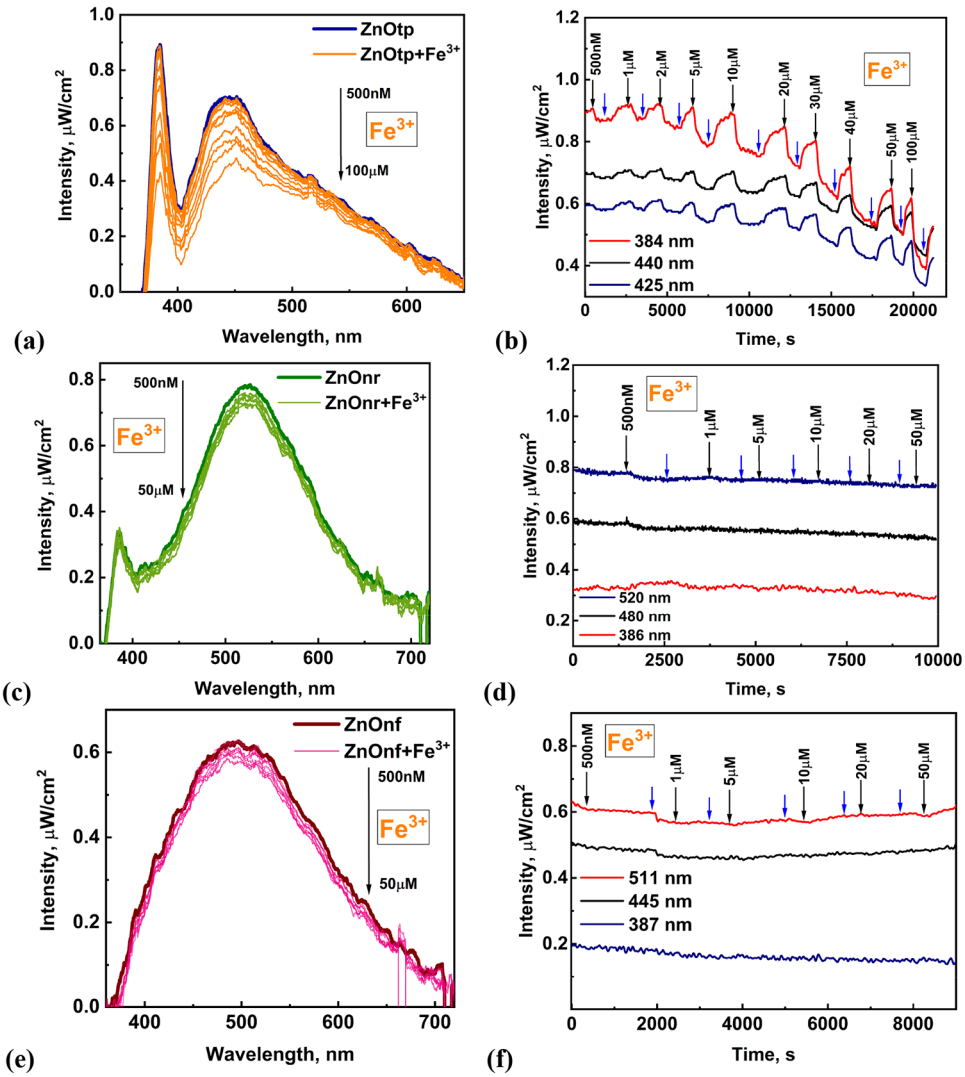

Figure 6. Sensitivity of ZnO structure-based sensors toward Fe^{3+} ions. Steady-state PL spectra (a, c, e) and kinetics of the PL (b, d, f) signal (the moment of adding the probe is marked with a black arrow, and the respective concentration is indicated; the moment when the cleaning process started is marked with a blue arrow).

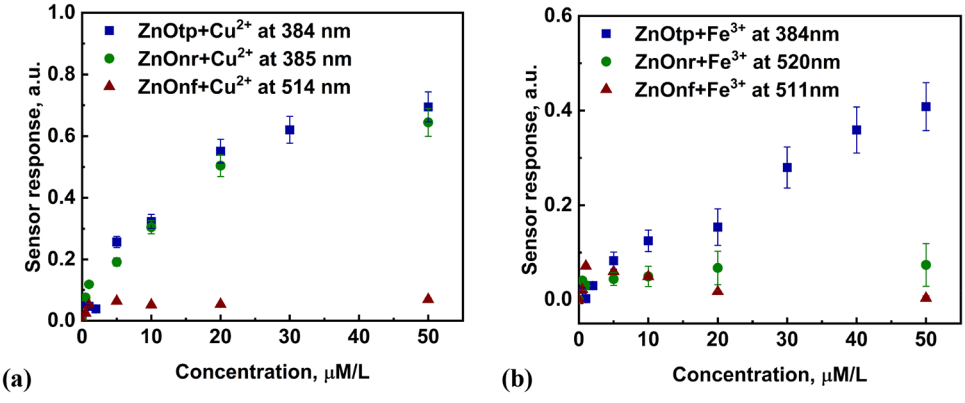

Figure 7. 1D ZnO sensor response to Cu^{2+} (a) and Fe^{3+} (b).

ions. Sensors based on ZnOtp nanostructures demonstrated good sensitivity toward Fe^{3+} ions in the range of 1−100 μM.

The intensities of the ZnOnr and ZnOnf PL in the UV and visible ranges of the spectra remained unchanged after interaction with Fe^{3+} ions (Figure 6c−f).

The sensor response curves of the 1D ZnO nanostructures to Cu^{2+} and Fe^{3+} ions are presented in Figure 7a,b, respectively. By using eq 4, we have calculated the values of the limit of detection of the sensors toward Cu^{2+} and Fe^{3+} ions. The obtained values are summarized in Table 4. From Table 4, we can conclude that ZnOnf did not show a sensor response to Cu^{2+} and Fe^{3+} ions.

https://doi.org/10.1021/acsanm.5c05081
ACS Appl. Nano Mater. 2026, 9, 3664−3678

Table 4. Comparison of Sensor Response to Cu^{2+} and Fe^{3+} Ions of 1D ZnO

parameter	ZnOtp		ZnOnr		ZnOnf	
	Cu^{2+}	Fe^{3+}	Cu^{2+}	Fe^{3+}	Cu^{2+}	Fe^{3+}
LOD	0.92 μM	1.4 μM	5.6 μM	-	-	-
time of sensor response	10.6 ± 2 min	10.9 ± 2 min	20 ± 2 min	-	-	-
noise/signal	2%	1.2%	3.7%	3.3%	4%	5.3%
standard deviation	2.3 × 10^{-5} μW/cm^2/nm	9.4 × 10^{-6} μW/cm^2/nm	3 × 10^{-5} μW/cm^2/nm	7.2 × 10^{-6} μW/cm^2/nm	1.6 × 10^{-5} μW/cm^2/nm	1.3 × 10^{-5} μW/cm^2/nm
linear range	5−20 μM	1−10 μM	2−20 μM			

ZnOnr showed a sensor response only to a high concentration of Cu^{2+} and no response to Fe^{3+} ions. ZnOtp showed a sensor response to both Cu^{2+} and Fe^{3+} ions.

The stability of the sensor signal and possible degradation of the ZnO PL in methanol were evaluated by the noise/signal ratio parameter, measured before the sensor tests. For all samples, the obtained values were lower than 5%, considering the high stability of the sensor signal.

The selectivity of 1D ZnO nanostructures was analyzed for 12 different metal ions (Figure 8a−c). The selectivity test was performed using the same fluidic system. A separate ZnO sensor was used for each type of ion. As a significant sensory response to Cu^{2+} and Fe^{3+} was observed for the studied nanostructures from 5 μM onward, a control concentration of 10 μM was chosen for the selectivity tests.

We calculated the Gibbs energy of Fe^{3+} adoption on ZnOtp and the Gibbs energy of Cu^{2+} on ZnOtp and ZnOnr (Figure 7a,b) by using the Langmuir and Langmuir−Freundlich isotherms. The obtained data are as follows: ΔG = −28.2 kJ/mol (ZnOtp to Cu^{2+}), ΔG = −23.7 kJ/mol (ZnOnr to Cu^{2+}), and ΔG = −22.3 kJ/mol (ZnOtp to Fe^{3+}). The Gibbs energies are in good agreement with sensor tests, showing a higher interaction between copper ions and the ZnO surface.

It was found that ZnOtp showed a significant response to Al^{3+} ions, whereas ZnOnr and ZnOnf did not show any sensor response to other metal ions. The PL of ZnO decreased after interaction with Al^{3+}. The sensor signal was reversible.

3.3. XPS Analysis. Mechanisms of Interaction between Metal Ions and the ZnO Surface

Sensor measurements showed irreversible adsorption of Cu^{2+} and Fe^{3+} ions at higher concentrations. In order to understand the sensor response and mechanisms of surface processes, XPS analyses were conducted after the sensing experiments. XPS was used to investigate the surface chemical composition and oxidation states of ZnOtp, ZnOnr, and ZnOnf before and after their interaction with Cu^{2+} and Fe^{3+} ions. The XPS data reflected the final surface chemical state rather than the cycle-resolved evolution. The XPS survey spectra (Figures 9a, S4a, and S5a) revealed prominent signals corresponding to Zn 2p and O 1s, along with additional peaks for C 1s, Zn 3s, Zn 3p, and Zn 3d, consistent with the expected ZnO stoichiometry. Upon Cu^{2+} incorporation, two additional peaks assigned to Cu 2p appeared in the Cu-ZnOtp and Cu-ZnOnr samples (Figures 9a and S4a), although with comparatively lower intensities, indicating successful copper integration into the ZnO matrix. The corresponding binding energies and peak assignments are summarized in Table S3. Likewise, the incorporation of Fe produced two new Fe 2p signals in Fe-ZnOtp and Fe-ZnOnr (Figures S6 and S7), confirming the presence of iron species, whereas no Fe or Cu peaks were detected in the ZnOnf-based samples (Figures S5, S7, and S8). The absence of detectable Cu and Fe signals in the ZnOnf structures likely reflects the morphological effects limiting dopant incorporation.

High-resolution Zn 2p spectra (Figures 9b, S4b, S5c, S6b,f, and S7b) consistently displayed two peaks at 1044 eV (Zn $2p_{1/2}$) and 1021 eV (Zn $2p_{3/2}$), with a binding energy separation of approximately 23.0 eV (Table S3), characteristic of Zn^{2+} in the ZnO lattice. These results confirm the absence of metallic Zn and the retention of the Zn^{2+} oxidation state following dopant incorporation.

The O 1s spectra (Figures 9c, S4c, S5b, S6c,g, and S7c) were deconvoluted into three components: lattice oxygen (O_{latt}^{2-})

https://doi.org/10.1021/acsanm.5c05081
ACS Appl. Nano Mater. 2026, 9, 3664−3678

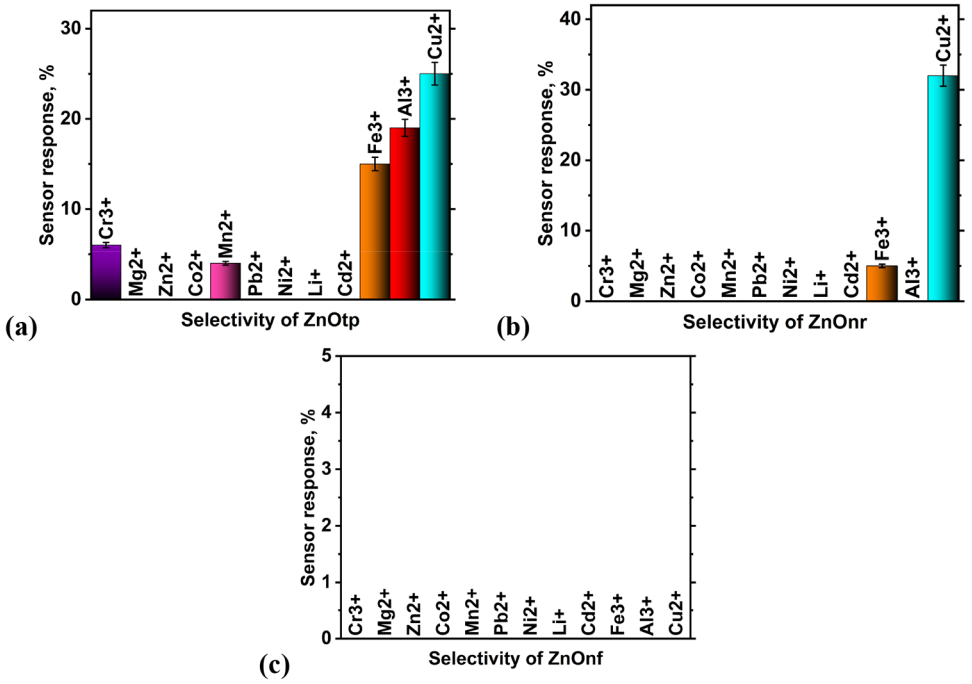

Figure 8. Selectivity results of the 1D ZnO nanostructures for metal cations: ZnOtp (a), ZnOnr (b), and ZnOnf (c).

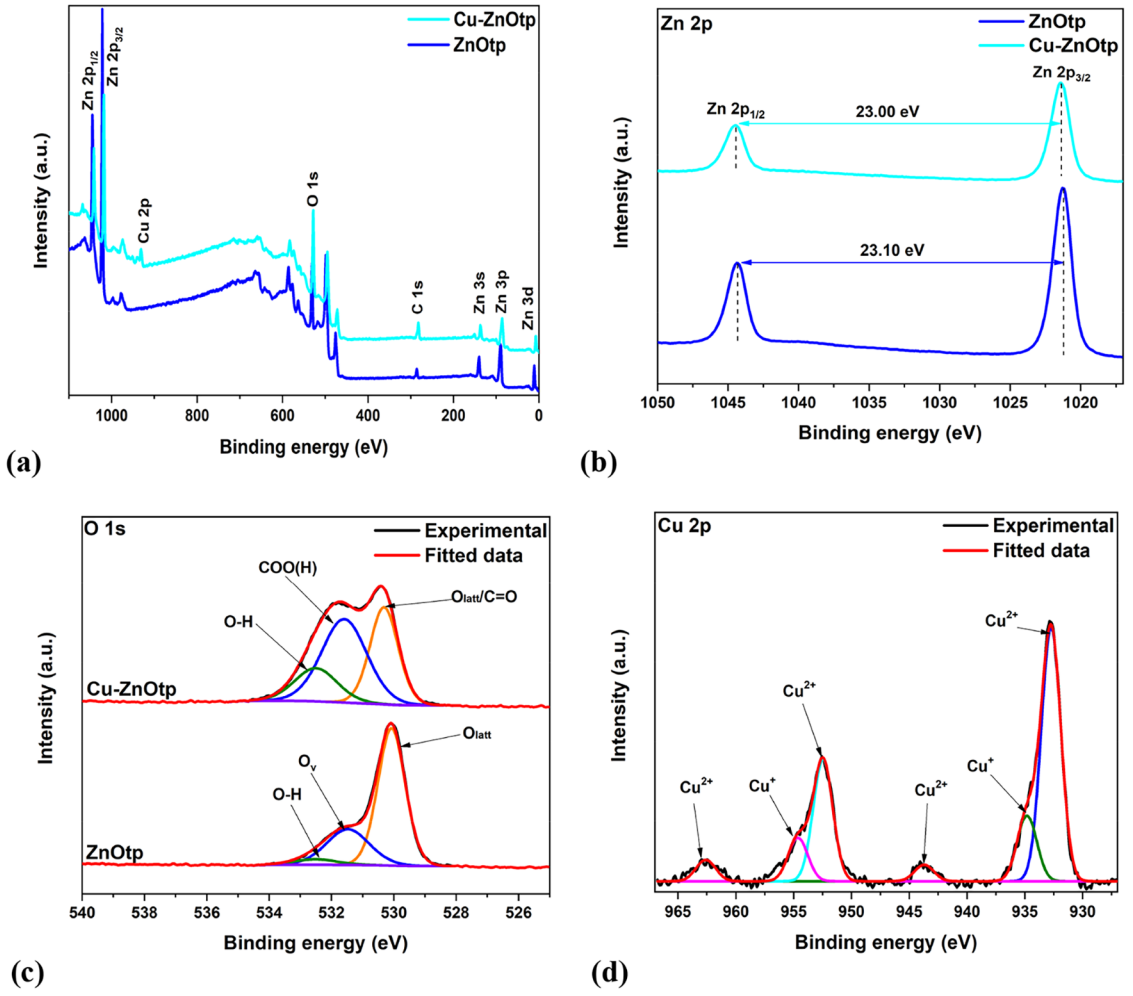

Figure 9. X-ray photoelectron spectra of Cu-ZnOtp and ZnOtp: survey (a), Zn 2p (b), O 1s (c), and Cu 2p (d).

https://doi.org/10.1021/acsanm.5c05081
ACS Appl. Nano Mater. 2026, 9, 3664−3678

centered near 530 eV, oxygen vacancies (O_v^{2-}) around 531 eV and, in Cu- and Fe-treated samples, additional contributions from oxygenated surface species such as COO(H) groups (Figure S8). The O_v component is associated with oxygen in defective or undercoordinated lattice environments, whereas the COO(H) contribution originates from surface-adsorbed species and is not related to intrinsic oxygen vacancies. Quantitative analysis of the O 1s components was performed by normalizing the fitted peak areas, and the corresponding ratios are summarized in Table S5 (Supporting Information). Pristine ZnO samples exhibit relatively low O_v/O_{latt} ratios (approximately 0.23−0.38 depending on the morphology), indicating a dominant lattice oxygen contribution. In contrast, Cu-modified ZnO shows a pronounced increase in defect-related oxygen species, with the O_v/O_{latt} ratios increasing up to approximately 0.5 and the $COO(H)/O_{latt}$ ratios exceeding unity for Cu-ZnOtp and Cu-ZnOnr, reflecting substantial surface modification induced by Cu incorporation. The Fe-modified ZnO samples display more moderate changes, with the O_v/O_{lat} ratios remaining below approximately 0.35, close to those of the corresponding pristine ZnO structures. These results demonstrate that both metal modification and ZnO morphology strongly influence the surface oxygen chemistry and defect population, which is consistent with their distinct sensing behaviors.[42]

High-resolution Cu 2p spectra (Figures 9d and Figure S4d) revealed Cu $2p_{3/2}$ peaks centered at approximately 932.7 eV and Cu $2p_{1/2}$ peaks at approximately 952.5 eV in Cu-ZnOtp and Cu-ZnOnr. Strong shakeup satellites observed at approximately 943−945 eV and approximately 962−963 eV are characteristic of Cu^{2+} species, conclusively ruling out metallic Cu, which lacks such features. Although the Cu $2p_{3/2}$ peak at 932.7 eV could overlap with Cu^+ (commonly reported near 932.5−933.0 eV), the pronounced satellite intensity confirms Cu^{2+} as the predominant oxidation state.[41,43]

A minor contribution from Cu^+ remains possible, as previously reported for similar ZnO-Cu systems, but is likely limited. XPS peak fitting (Table S4) quantified Cu^{2+} contributions of 80.7% for Cu-ZnOnr and 79.4% for Cu-ZnOtp in the Cu $2p_{3/2}$ region, with corresponding Cu^+ contents of 19.4% and 20.6%, respectively. In the Cu $2p_{1/2}$ region, Cu^{2+} comprised 73.7% in Cu-ZnOnr and 73.9% in Cu-ZnOtp, while Cu^+ accounted for 35.8% and 26.2%, respectively. These results provide direct evidence for the partial reduction of Cu^{2+} to Cu^+ on the ZnO surface.[44,45]

High-resolution Fe 2p spectra (Figure S6d, S5h, and S8) exhibited Fe $2p_{3/2}$ peaks at 710.6 and 710.3 eV and Fe $2p_{1/2}$ peaks at 723.8 and 723.5 eV for Fe-ZnOnr and Fe-ZnOtp, respectively, along with pronounced shakeup satellites at approximately 718 eV. Deconvolution of the Fe $2p_{3/2}$ region revealed peaks at 710.3 eV (Fe^{2+}) and 712.3 eV (Fe^{3+}) in Fe-ZnOnr, with respective contributions of 63.2% and 27.7%. In Fe-ZnOtp, peaks at 710.0 eV (Fe^{2+}) and 711.8 eV (Fe^{3+}) yielded Fe^{2+} at 77.9% and Fe^{3+} at 22.8%. These results indicate a clear predominance of Fe^{2+} species in both nanostructures, in agreement with the literature, where Fe^{2+} is favored due to its ionic radius (0.78 Å) closely matching that of Zn^{2+} (0.74 Å), promoting substitutional incorporation into the ZnO lattice.[46]

Overall, XPS analysis provides clear spectroscopic evidence for the surface-assisted reduction of Cu^{2+} to Cu^+ and Fe^{3+} to Fe^{2+} on 1D ZnO nanostructures. These findings correlate well with the observed color change of ZnOtp after interaction with Cu^{2+} ions (Figure S3). The XPS results fit well with the sensor results measured by PL spectroscopy. The irreversible signal of ZnOtp at a high concentration of Fe^{3+} ions is explained by the formation of Fe^{3+} centers on the ZnO surface and their reduction to Fe^{2+}. The XPS findings confirm the presence of Fe^{3+} centers in the Fe-ZnOnr and Fe-ZnOtp samples. Although Fe^{2+} was quantitatively dominant based on XPS (63.2% and 77.9%, respectively), the contribution of the Fe^{3+} species (27.7% and 22.8%) was evident. The PL sensor response highlighted a decrease of intensity through defect-mediated recombination processes. Combined XPS and PL analyses showed that copper is primarily incorporated as Cu^{2+}, with a minor Cu^+ fraction. These mixed oxidation states, along with structural defects (vacancies) and surface hydroxyl groups, are expected to modulate the electronic, catalytic, and sensing properties of ZnO-based nanostructures.

The interaction mechanisms between ZnO surfaces and metal ions differ for ZnOnf, ZnOnr, and ZnOtp. UV photoexcitation increases the concentration of electrons and holes. This will reduce the depletion layer (Table 3) and provide better ion transfer to the surface. The thinner depletion layer in ZnOtp (15.3 nm in air) compared to those in ZnOnr (18.0 nm) and ZnOnf (17.9 nm) enables more efficient charge transfer, contributing to its superior sensing performance (Table 4).

The interactions between Cu^{2+} and Fe^{3+} ions and the ZnO surface are different due to the properties of the ions and mechanisms of interaction, which depend on the surface charge (Figure 4), depletion layer width (Table 3), and types of defects present in the ZnO nanostructures.

ZnO is a typical surface for photoactivated reduction of Cu^{2+} ions on the surface of ZnO.[47,48] Cu^{2+} ions capture free electrons and transform them into neutral Cu^0

$$Cu^{2+} + 2e^- \rightarrow Cu^0 \tag{6a}$$

Defects can facilitate Cu^{2+} reduction. As the ion radii of Zn^{2+} and Cu^{2+} ions are similar, Cu^{2+} could substitute Zn^{2+} or take place in Zn vacancies.[49] It was shown that Zn interstitials could participate in Cu^{2+} reduction as[49]

$$Zni^{2+} + 2e^- + Cu^{2+} \rightarrow Cu^0 + Zn^{2+} \tag{6b}$$

One of the alternative interaction mechanisms has a couple of stages. Initially, Cu^{2+} could adsorb on the negatively charged ZnO surface.[50] Then, interaction with water or surface oxygen leads to the formation of CuO/Cu_2O[51]

$$ZnO + Cu^{2+} \rightarrow ZnO/Cu^{2+} \tag{6c}$$

$$ZnO/Cu^{2+} + 2OH^- \rightarrow ZnO/Cu(OH)_2 \tag{6d}$$

$$ZnO/Cu(OH)_2 \rightarrow ZnO/CuO + H_2O \tag{6e}$$

XPS analysis of ZnOtp and ZnOnr showed that Cu was present in the 2+/1+ states. This means that Cu^{2+} reduction is less favorable, and copper oxide is formed. The formation of CuO/Cu_2O on the ZnO surface can involve lattice oxygen or surface, thus forming additional oxygen vacancies or surface hydroxyl groups.[52,53] At the same time, CuO/Cu_2O absorbs light in the UV−vis region, quenches PL, and separate photogenerated charges.[54] Therefore, the most reliable mechanism of interaction between ZnO and Cu^{2+} ions is the formation of ZnO−copper oxide composite. The sensitivity toward Cu^{2+} ions is defined by the ζ-potential, depletion layer, and structure defects in the ZnO nanostructures. The decrease in the PL intensity and growth of the O 1s XPS peak after

https://doi.org/10.1021/acsanm.5c05081
ACS Appl. Nano Mater. 2026, 9, 3664−3678

Table 5. Comparison of $Cu^{2+}$and Fe^{3+} Sensing by 1D ZnO Nanostructures vs Literature Data[a]

material/structure	detection method	Cu^{2+} LOD, μM	Fe^{3+} LOD, μM	response time	selectivity	stability (noise/signal)	key advantage
ZnOtp (this work)	PL	0.92	1.4	10.6 ± 2 min	excellent (12 ions tested)	good (2.0)	dual sensitivity to Cu^{2+} and Fe^{3+}; lowest Fe^{3+} LOD; best SNR
ZnOnr (this work)	PL	5.6	N.D.	20 ± 2 min	excellent (12 ions tested)	good (3.7)	Cu^{2+} selective; comparable response time
ZnOnf (this work)	PL	N.R.	N.D.	N.R.	N.R.	N.A.	reference (morphology unsuitable)
ZnO nanorods[64]	PL	0.1−1	5−50	5−30 min	not reported	not reported	broad concentration range
ZnO nanoparticles[64]	PL	1−5	10−50	10−30 min	not reported	not reported	simple synthesis method
Au-decorated ZnO[65]	PL	<0.1	N.D.	5−15 min	not reported	not reported	ultrahigh Cu^{2+} sensitivity (plasmonic)
plasmonic Au-ZnO[61,66]	photocatalytic	ppm	N.D.	5−20 min	not reported	not reported	plasmonic enhancement mechanism
ZnO@MOF-5[67]	FL	0.1	N.D.	time-dependent	not reported	not reported	MOF composite; 96% efficiency

[a]**N.R.** = no response; **N.A.** = not applicable; N.D. = not definable; **PL** = photoluminescence; **FL** = fluorescence.

interaction with Cu^{2+} result from the formation of copper oxide and nonstoichiometric surface oxygen.

The interaction of ZnO with Fe^{3+} is based on the adsorption of Fe^{3+} ions.[55,56] It was shown that Fe^{3+} can be incorporated into the ZnO lattice. The key factor in the interaction is the neutral oxygen vacancy.

Fe^{3+} ions form complexes with oxygen or zinc vacancies. The PL intensity decreased after the formation of Fe^{3+}/Fe^{2+} complexes on the ZnO surface. This leads to a decrease of PL in the range of 380−500 nm, not changing the PL spectra at 500−550 nm.[57] Therefore, the response of ZnO to Fe^{3+} would depend on the specific type of defects in ZnO and, perhaps, the ζ-potential of the ZnO surface.

The reversible response of ZnOtp toward Al^{3+} ions was demonstrated. We propose the following interaction mechanism between ZnO and Al^{3+}. As Al^{3+} ionic radii (0.55 nm) are sufficiently smaller than those of Zn^{2+} (0.74 nm), Al^{3+} ions could diffuse to the ZnO surface and capture electrons.[58,59]

In contrast to Fe, which is a d-material, Al has only s and p electron orbitals and one type of ionized state 3+. No reduction reactions are possible upon interaction with ZnO. Therefore, Al^{3+} mainly desorbs from the ZnO surface, resulting in a reversible reaction.

The structure and optical properties play important roles in the sensor response. The ζ-potential (Figure 4) and XPS analyses of surface-adsorbed oxygen show a higher concentration of molecular oxygen in ZnOtp and ZnOnr, and therefore, a negative surface charge. The hole-scavenging effect of ZnO immersed in methanol significantly changes the properties of ZnOtp due to its smaller diameter (Table 1) and depletion layer width (Table 3, 15.3 nm in air). The shift in the PL peak, explained by the possible change in the charge of the defect states in ZnO, could be a reason for the higher sensor response to Fe^{3+} in ZnOtp, compared to ZnOnr and ZnOnf.

The sensing properties of the 1D ZnO nanostructures fit well with the detection of metal ions of ZnO sensors reported in the literature.[60,61] The LOD values obtained for ZnOtp (Cu^{2+}: 0.92 μM, Fe^{3+}: 1.4 μM) are compatible with the sensor parameters reported for other ZnO-based sensors. The sensor response time observed for all morphologies is competitive with literature values, where most ZnO sensors require 5−30 min for stable signal development.[60,62,63] A comparison of the investigated 1D ZnO nanomaterials with existing sensors is summarized in Table 5.

The results obtained in the present work showed competitive sensor properties compared to other ZnO optical chemical sensors, as reported in Table 5. The main challenges of ZnO optical chemical sensors are selectivity and their lower LOD. One of the future tendencies is the development of ZnO−ligand composites.[68] The present work is highly important for future trends in the detection of metal ions by using ZnO−ligand composites. In order to avoid nonspecific interactions between ZnO and metal ions in ZnO−ligand composites, it is important to evaluate the sensitivity of bare ZnO nanostructures to metal ions and validate the sensitivity range, LOD, and selectivity. Ion formation will completely change the sensor response of the ZnO−ligand composites toward the metal ions. The engineering and control of all sensor components will enable the development of low-cost and selective optical chemical sensors for metal ion detection on the basis of 1D ZnO PL nanostructures.

4. CONCLUSIONS

This study provides a comprehensive analysis of the structural, optical, and surface properties of three different nanostructures and describes the direct relationship between these properties and the sensor properties of the investigated nanomaterials.

This study demonstrates that 1D ZnO nanostructures enable the detection of Cu^{2+} and Fe^{3+} ions using PL spectroscopy. ZnOtp achieves detection limits of 0.92 and 1.4 μM to Cu^{2+} and Fe^{3+} ions, respectively, thus surpassing the performance of most reported ZnO-based sensors. For instance, ZnOtp showed the highest adsorption capacity for different metal ions due to its higher surface charge. The sensor properties of the 1D ZnO nanostructures are tailored by their structural, electronic, and optical properties. The interaction mechanism between the ZnO surface and metal ions is based on chemical interactions and exhibits irreversible behavior. The mechanism involves the adsorption of metal ions on the ZnO surface, capture of photogenerated free electrons, and reduction to a neutral state. The interaction mechanism between ZnO surfaces and metal ions is experimentally validated by XPS and PL analyses and is based on irreversible adsorption, charge transfer, formation of CuO/Cu_2O, and partial reduction of Fe^{3+} to Fe^{2+} on the ZnO surface. The adsorption states on the surfaces of 1D ZnO nanostructures are defined by natural defects. The calculated Gibbs energies showed a higher affinity of the ZnO nanostructures toward Cu^{2+} ions than toward Fe^{3+} ions.

https://doi.org/10.1021/acsanm.5c05081
ACS Appl. Nano Mater. 2026, 9, 3664−3678

The sensor properties of the 1D ZnOtp are compatible with other ZnO nanostructures applied for metal ion detection. The demonstrated detection capabilities have significant practical implications in environmental monitoring, agricultural applications, and industrial process control. It is evident that the sensors demonstrate considerable potential for utilization in the real-time evaluation of water quality, given that their detection limits are well below the WHO guidelines for drinking water (31.5 μM for Cu, 5.4 μM for Fe). The relatively rapid response times (10.6−10.9 ± 2 min) and good selectivity against interfering ions make them suitable for integration into automated monitoring systems.

Despite good sensor responses to copper and iron ions, additional sensitivities to aluminum ions have been identified. The irreversible sensor response opens perspectives for a one-use detection strategy. As ZnO is a good and stable nanotemplate with advanced optical properties, the observed effects could be used for other sensor applications, like forming ZnO−Cu and ZnO−Fe composites. The incorporated metal and metal oxide clusters could be templated for the growth of advanced selective composites for sensor and photocatalysis applications.

■ ASSOCIATED CONTENT

Supporting Information

The Supporting Information is available free of charge at https://pubs.acs.org/doi/10.1021/acsanm.5c05081.

Size distribution of the investigated ZnO nanostructures (Figure S1); linear dimension and specific surface area (SSA) evaluation of the ZnO nanostructures (Table S1); deconvolution of 1D ZnO PL spectra and PL temperature dependence of ZnOtp (Figure S2); 1D ZnO PL deconvolution analysis (Table S2); pictures of ZnOtp samples before and after sensor testing toward Cu^{2+} ions (Figure S3); X-ray photoelectron spectra of Cu-ZnOnr and ZnOnr (Figure S4); XPS spectra of ZnOnf and Cu-ZnOnf (Figure S5); X-ray photoelectron spectra of Fe-ZnOnr and ZnOnr (Figure S6); XPS spectra of ZnOnf and ZnOnf (Figure S7); binding energy values (eV) for Zn 2p, O 1s, and Cu 2p peaks in ZnO, and their Cu- and Fe-incorporated compounds (Table S3); quantitative XPS analysis of Cu 2p and Fe 2p core-level spectra (Table S4); quantitative XPS analysis of O 1s core-level spectra (Table S5); binding energy values (eV) for C 1s peaks in ZnOnr, ZnOnf, ZnOtp, and their Cu- and Fe-incorporated compounds (Table S6); high-resolution XPS spectra of C 1s and Fe 2p for Fe−ZnO samples (Figure S8); FTIR spectra of ZnOtp, ZnOtp+Cu^{2+} (Figure S9); ZnOtp PL spectra during the selectivity test and kinetics of the reaction (Figure S10); ZnOnr PL spectra during the selectivity test and kinetics of the reaction (Figure S11); diffuse reflectance of samples (Figure S12); electron paramagnetic resonance (EPR) spectrum of ZnOtp at room temperature (Figure S13) (PDF)

■ AUTHOR INFORMATION

Corresponding Authors

Roman Viter − *Institute of Atomic Physics and Spectroscopy, Faculty of Science and Technology, University of Latvia, LV-1004 Riga, Latvia;* orcid.org/0000-0002-9996-041X; Email: roman.viter@lu.lv

Arunas Ramanavicius − *Department of Nanotechnology, State Research Institute Center for Physical and Technological Sciences, LT-10257 Vilnius, Lithuania; Department of Physical Chemistry, Faculty of Chemistry and Geosciences, Vilnius University, 03225 Vilnius, Lithuania;* orcid.org/0000-0002-0885-3556; Email: arunas.ramanavicius@chf.vu.lt

Authors

Iryna Tepliakova − *Institute of Atomic Physics and Spectroscopy, Faculty of Science and Technology, University of Latvia, LV-1004 Riga, Latvia;* orcid.org/0000-0002-6234-535X

Mahmoud Abid − *Institut Européen des Membranes (IEM), UMR 5635, CNRS−Université de Montpellier−ENSCM, 34293 Montpellier, France*

Simas Rackauskas − *Institute of Materials Science, Kaunas University of Technology, 51423 Kaunas, Lithuania;* orcid.org/0000-0002-8964-5299

Mikhael Bechelany − *Institut Européen des Membranes (IEM), UMR 5635, CNRS−Université de Montpellier−ENSCM, 34293 Montpellier, France;* orcid.org/0000-0002-2913-2846

Complete contact information is available at: https://pubs.acs.org/10.1021/acsanm.5c05081

Author Contributions

The manuscript was written through the contributions of all authors. All authors have given approval to the final version of the manuscript.

Funding

This Research was supported by the European Research Executive Agency (REA) project **SENS4CORN** No **101086364.**

Notes

The authors declare no competing financial interest.

■ ACKNOWLEDGMENTS

S.R. acknowledges funding from the Research Council of Lithuania (Project No. S-ITP-24-4).MB "SensoGrafa" (Prof. habil. dr. Arunas Ramanavicius and PhD student Greta Zvirzdine) for assistance in carying out the experimental part of the work, which was supported by European Research Executive Agency (REA) project **SENS4CORN** No **101086364**. Figure [1] "The principal scheme of fluidic system integrated with photoluminescence setup" created in BioRender. Tepliakova, I. (https://BioRender.com/q2v8dju) is licensed under CC BY 4.0. "Table of Content (TOC)" created in BioRender. Tepliakova, I. (https://BioRender.com/ucuyw6y) is licensed under CC BY 4.0.

■ REFERENCES

(1) Mahesh, A.; Kumar, G. P.; Jawahar, I. N.; Biju, V. Temperature Dependent Photoluminescence Spectra of Nanocrystalline Zinc Oxide: Effect of Processing Condition on the Excitonic and Defect Mediated Emissions. *Chem. Phys. Impact* **2024**, *8*, No. 100456.

(2) Viter, R.; Khranovskyy, V.; Starodub, N.; Ogorodniichuk, Y.; Gevelyuk, S.; Gertnere, Z.; Poletaev, N.; Yakimova, R.; Erts, D.; Smyntyna, V.; Ubelis, A. Application of Room Temperature Photoluminescence from ZnO Nanorods for Salmonella Detection. *IEEE Sens. J.* **2014**, *14* (6), 2028−2034.

(3) Dhiman, V.; Kondal, N. ZnO Nanoadsorbents: A Potent Material for Removal of Heavy Metal Ions from Wastewater. *Colloid Interface Sci. Commun.* **2021**, *41*, No. 100380.
(4) Chen, X.; Wang, Q.; Wang, X.-J.; Li, J.; Xu, G.-B. Synthesis and Performance of ZnO Quantum Dots Water-Based Fluorescent Ink for Anti-Counterfeiting Applications. *Sci. Rep.* **2021**, *11* (1), No. 5841.
(5) Chen, K.; Liu, Y.; Fu, Y.; Huang, J.; Feng, X.; Wang, J.; Zhai, M.; Lupoi, R.; Yin, S.; Li, H. Loading of Zn/ZnO Particles in the Precursor Feedstock Affects the Characteristics of Liquid Plasma Sprayed Nano-ZnO Coatings for Photocatalytic Applications. *Nanotechnology* **2020**, *31* (18), No. 185301.
(6) Chu, Y.-L.; Young, S.-J.; Liu, C.-J.; Arya, S.; Chu, T.-T. Enhanced UV-Sensing Performances of 2-D Pd/ZnO Nanosheet Photodetectors through Inexpensive Photochemical Synthesis at Room Temperature and Their Humidity Applications. *ACS Appl. Electron. Mater.* **2025**, *7* (1), 129−142.
(7) Godse, P. R.; Kadam, S. A.; Nimbalkar, T. M.; Jadhav, Y. M.; Jadhao, Y. B.; Ma, Y.-R.; Patil, V. B. Ultra-Responsive and Highly Sensitive 1D ZnO Nanotubes for Detecting Perilous Low Levels of NO2 Gas. *Mater. Adv.* **2024**, *5* (7), 2826−2840.
(8) Viter, R.; Savchuk, M.; Iatsunskyi, I.; Pietralik, Z.; Starodub, N.; Shpyrka, N.; Ramanaviciene, A.; Ramanavicius, A. Analytical, Thermodynamical and Kinetic Characteristics of Photoluminescence Immunosensor for the Determination of Ochratoxin A. *Biosens. Bioelectron.* **2018**, *99*, 237−243.
(9) Viter, R.; Savchuk, M.; Starodub, N.; Balevicius, Z.; Tumenas, S.; Ramanaviciene, A.; Jevdokimovs, D.; Erts, D.; Iatsunskyi, I.; Ramanavicius, A. Photoluminescence Immunosensor Based on Bovine Leukemia Virus Proteins Immobilized on the ZnO Nanorods. *Sens. Actuators, B* **2019**, *285*, 601−606.
(10) Turemis, M.; Zappi, D.; Giardi, M. T.; Basile, G.; Ramanaviciene, A.; Kapralovs, A.; Ramanavicius, A.; Viter, R. ZnO/Polyaniline Composite-Based Photoluminescence Sensor for the Determination of Acetic Acid Vapor. *Talanta* **2020**, *211*, No. 120658.
(11) Zhang, S.; Ling, W.; Zhao, T.; Pu, Y.; Cao, S.; Zhu, D. High Response ZnO Gas Sensor Derived from Tb@Zn-MOFs to Acetic Acid under UV Excitation. *Sens. Actuators, A* **2024**, *365*, No. 114862.
(12) Kumar, M.; Chauhan, M. S.; Akhtar, M. S.; Umar, A. Effect of Cerium Ions in Ce-Doped ZnO Nanostructures on Their Photocatalytic and Picric Acid Chemical Sensing. *Ceram. Int.* **2021**, *47* (3), 3089−3098.
(13) Kumar, M.; Negi, K.; Umar, A.; Chauhan, M. S. Photocatalytic and Fluorescent Chemical Sensing Applications of La-Doped ZnO Nanoparticles. *Chem. Pap.* **2021**, *75* (4), 1555−1566.
(14) Kumar, R.; Umar, A.; Kumar, R.; Chauhan, M. S. Al-Hadeethi, Y. ZnO−SnO_2 Nanocubes for Fluorescence Sensing and Dye Degradation Applications. *Ceram. Int.* **2021**, *47* (5), 6201−6210.
(15) Leal, A. N. R.; Brandão, W. Q.; de Aguiar, M. F.; Kór, D. G.; França, E. L. T.; de Melo, C. P.; de Almeida, Y. M. B. Utilizing Green Zinc Oxide Nanoparticles as a Sensing Platform for Ascorbic Acid. *Talanta* **2024**, *280*, No. 126769.
(16) Guo, Y.; Zhang, Y.; Li, T.; Tao, T. ZnO Quantum Dots for Fluorescent Detection of Environmental Contaminants. *J. Environ. Chem. Eng.* **2021**, *9* (6), No. 106800.
(17) Gangopadhyay, B.; Subash, J.; Saha, N.; Hussain, S.; Pal, S.; Mukherjee, S.; Hawaldar, R.; Hazra, S.; Chattopadhyay, D. Low-Temperature Base-Catalyzed Si-Capped ZnO Quantum Dots for pH-Switchable Dual Sensing of Amoxicillin and Cr3+. *ACS Appl. Nano Mater.* **2024**, *7* (17), 20829−20840.
(18) Islam, S. U.; Latief, U.; Ali, J.; Khan, M. S. Long Wavelength Emissive ZnO/CQDs Phosphor with High Color Purity and Its Application in Sensitive Detection of Cadmium(II). *Spectrochim. Acta, Part A* **2024**, *304*, No. 123292.
(19) Yang, X.; Li, Z.; Liu, N.; Song, W.; Sun, Q.; Xie, Y. Fabrication of Hydrophilic Luminescent Zinc Oxide Quantum Dots for Selective Detection of Copper Ions and Efficient Inhibition of Harmful Fungi. *Arab. J. Chem.* **2022**, *15* (11), No. 104266.
(20) Khan, M. M. R.; Mitra, T.; Sahoo, D. Metal Oxide QD-Based Ultrasensitive Microsphere Fluorescent Sensor for Copper, Chromium and Iron Ions in Water. *RSC Adv.* **2020**, *10* (16), 9512−9524.
(21) Wu, W. J.; Zhao, Q.; Zhou, R.; Liang, Y. C.; Zhao, W. B.; Shan, C. X. Ratiometric Fluorescence Sensor Based on Europium-Grafted ZnO Quantum Dots for Visual and Colorimetric Detection of Tetracycline. *Spectrochim. Acta, Part A* **2021**, *259*, No. 119901.
(22) Zolotko, A. N.; Poletaev, N. I.; Vovchuk, Y. I. Gas-Disperse Synthesis of Metal Oxide Particles. *Combust., Explos. Shock Waves* **2015**, *51* (2), 252−268.
(23) Rackauskas, S.; Klimova, O.; Jiang, H.; Nikitenko, A.; Chernenko, K. A.; Shandakov, S. D.; Kauppinen, E. I.; Tolochko, O. V.; Nasibulin, A. G. A Novel Method for Continuous Synthesis of ZnO Tetrapods. *J. Phys. Chem. C* **2015**, *119* (28), 16366−16373.
(24) Ilickas, M.; Mardosaite, R.; Cesano, F.; Cravanzola, S.; Barolo, C.; Scarano, D.; Viscardi, G.; Rackauskas, S. ZnO Tetrapod Morphology Influence on UV Sensing Properties. *Nanotechnology* **2024**, *35* (1), No. 015502.
(25) Sulciute, A.; Nishimura, K.; Gilshtein, E.; Cesano, F.; Viscardi, G.; Nasibulin, A. G.; Ohno, Y.; Rackauskas, S. ZnO Nanostructures Application in Electrochemistry: Influence of Morphology. *J. Phys. Chem. C* **2021**, *125* (2), 1472−1482.
(26) Iatsunskyi, I.; Vasylenko, A.; Viter, R.; Kempiński, M.; Nowaczyk, G.; Jurga, S.; Bechelany, M. Tailoring of the Electronic Properties of ZnO−Polyacrylonitrile Nanofibers: Experiment and Theory. *Appl. Surf. Sci.* **2017**, *411*, 494−501.
(27) Chaaya, A. A.; Bechelany, M.; Balme, S.; Miele, P. ZnO 1D Nanostructures Designed by Combining Atomic Layer Deposition and Electrospinning for UV Sensor Applications. *J. Mater. Chem. A* **2014**, *2* (48), 20650−20658.
(28) Viter, R.; Iatsunskyi, I.; Fedorenko, V.; Tumenas, S.; Balevicius, Z.; Ramanavicius, A.; Balme, S.; Kempiński, M.; Nowaczyk, G.; Jurga, S.; Bechelany, M. Enhancement of Electronic and Optical Properties of ZnO/Al_2O_3 Nanolaminate-Coated Electrospun Nanofibers. *J. Phys. Chem. C* **2016**, *120* (9), 5124−5132.
(29) Bandopadhyay, K.; Mitra, J. Zn Interstitials and O Vacancies Responsible for N-Type ZnO: What Do the Emission Spectra Reveal? *RSC Adv.* **2015**, *5* (30), 23540−23547.
(30) Tam, K. H.; Cheung, C. K.; Leung, Y. H.; Djurišić, A. B.; Ling, C. C.; Beling, C. D.; Fung, S.; Kwok, W. M.; Chan, W. K.; Phillips, D. L.; Ding, L.; Ge, W. K. Defects in ZnO Nanorods Prepared by a Hydrothermal Method. *J. Phys. Chem. B* **2006**, *110* (42), 20865−20871.
(31) Gurylev, V.; Perng, T.-P. Defect Engineering of ZnO: Review on Oxygen and Zinc Vacancies. *J. Eur. Ceram. Soc.* **2021**, *41* (10), 4977−4996.
(32) Fedorenko, V.; Viter, R.; Mrówczyński, R.; Damberga, D.; Coy, E.; Iatsunskyi, I. Synthesis and Photoluminescence Properties of Hybrid 1D Core−Shell Structured Nanocomposites Based on ZnO/Polydopamine. *RSC Adv.* **2020**, *10* (50), 29751−29758.
(33) Damberga, D.; Viter, R.; Fedorenko, V.; Iatsunskyi, I.; Coy, E.; Graniel, O.; Balme, S.; Miele, P.; Bechelany, M. Photoluminescence Study of Defects in ZnO-Coated Polyacrylonitrile Nanofibers. *J. Phys. Chem. C* **2020**, *124* (17), 9434−9441.
(34) Torchynska, T.; El Filali, B.; Polupan, G.; Shcherbyna, L. Emission, Defects and Structure of ZnO Nanocrystals Obtained by Electrochemical Method. *MRS Adv.* **2017**, *2* (43), 2343−2348.
(35) Vempati, S.; Mitra, J.; Dawson, P. One-Step Synthesis of ZnO Nanosheets: A Blue−White Fluorophore. *Nanoscale Res. Lett.* **2012**, *7* (1), No. 470.
(36) Zeng, H.; Duan, G.; Li, Y.; Yang, S.; Xu, X.; Cai, W. Blue Luminescence of ZnO Nanoparticles Based on Non-Equilibrium Processes: Defect Origins and Emission Controls. *Adv. Funct. Mater.* **2010**, *20* (4), 561−572.
(37) Huang, Y.-L.; Chiu, S.-P.; Zhu, Z.-X.; Li, Z.-Q.; Lin, J.-J. Variable−Range−Hopping Conduction Processes in Oxygen Deficient Polycrystalline ZnO Films. *J. Appl. Phys.* **2010**, *107* (6), No. 063715.
(38) Liao, Z.-M.; Zhang, H.-Z.; Zhou, Y.-B.; Xu, J.; Zhang, J.-M.; Yu, D.-P. Surface Effects on Photoluminescence of Single ZnO Nanowires. *Phys. Lett. A* **2008**, *372* (24), 4505−4509.

https://doi.org/10.1021/acsanm.5c05081
ACS Appl. Nano Mater. 2026, 9, 3664−3678

(39) Wu, K.; Jia, Z.; Zhou, L.; Yuan, S.; Cui, J. Study on the Effect of Methanol on the Morphology and Optical Properties of ZnO. *Optik* **2020**, *205*, No. 164250.
(40) Marin, O.; González, V.; Tirado, M.; Comedi, D. Effects of Methanol on Morphology and Photoluminescence in Solvothermal Grown ZnO Powders and ZnO on Si. *Mater. Lett.* **2019**, *251*, 41−44.
(41) Maldonado-Arriola, J. A.; Sánchez-Zeferino, R.; Álvarez-Ramos, M. E. Photoluminescent Properties of ZnO Nanorods Films Used to Detect Methanol Contamination in Tequila. *Sens. Actuators, A* **2020**, *312*, No. 112142.
(42) Lin, C.; Zhang, H.; Zhang, J.; Chen, C. Enhancement of the Humidity Sensing Performance in Mg-Doped Hexagonal ZnO Microspheres at Room Temperature. *Sensors* **2019**, *19* (3), No. 519.
(43) Aadnan, I.; Zegaoui, O.; El Mragui, A.; Moussout, H.; Esteves da Silva, J. C. G. Structural, Optical and Photocatalytic Properties under UV-A and Visible Lights of Co-, Ni- and Cu-Doped ZnO Nanomaterials: Comparative Study. *Arab. J. Chem.* **2024**, *17* (1), No. 105336.
(44) Ghodselahi, T.; Vesaghi, M. A.; Shafiekhani, A.; Baghizadeh, A.; Lameii, M. XPS Study of the Cu@Cu_2O Core−Shell Nanoparticles. *Appl. Surf. Sci.* **2008**, *255* (5), 2730−2734.
(45) de Sousa, P. V. F.; de Oliveira, A. F.; da Silva, A. A.; Lopes, R. P. Environmental Remediation Processes by Zero Valence Copper: Reaction Mechanisms. *Environ. Sci. Pollut. Res.* **2019**, *26* (15), 14883−14903.
(46) Halligudra, G.; Shivaramu, P. D.; Paramesh, C. C.; Roy, K.; Sabbanahalli; Rangappa, D.; et al. Enhanced Catalytic Reduction and Electrochemical Sensing Properties of Magnetic Fe_3O_4@benzothiazole-Cu(II) Nanoparticles. *J. Inorg. Organomet. Polym. Mater.* **2024**, *34* (9), 4349−4363.
(47) Moussa, H.; Merlin, C.; Dezanet, C.; Balan, L.; Medjahdi, G.; Ben-Attia, M.; Schneider, R. Trace Amounts of Cu2+ Ions Influence ROS Production and Cytotoxicity of ZnO Quantum Dots. *J. Hazard. Mater.* **2016**, *304*, 532−542.
(48) Singh, A.; Wan, F.; Yadav, K.; Salvi, A.; Thakur, P.; Thakur, A. Synergistic Effect of ZnO Nanoparticles with Cu^{2+} Doping on Antibacterial and Photocatalytic Activity. *Inorg. Chem. Commun.* **2023**, *157*, No. 111425.
(49) Li, Q.; Wang, C. Cu Nanostructures Formed via Redox Reaction of Zn Nanowire and Cu^{2+}-Containing Solutions. *Chem. Phys. Lett.* **2003**, *375* (5−6), 525−531.
(50) Bagtache, R.; Missaoui, A.; Korib, A.; Brahimi, R.; Trari, M. The Cu^{2+} Reduction and H_2 Evolution on the Hetero-System CuFeO2/ZnO under Visible Light. *Appl. Water Sci.* **2020**, *10* (6), No. 134.
(51) Meena, P. L.; Poswal, K.; Surela, A. K. Fabrication of ZnO/CuO Hybrid Nanocomposite for Photocatalytic Degradation of Brilliant Cresyl Blue (BCB) Dye in Aqueous Solutions. *J. Water Environ. Nanotechnol.* **2021**, *6* (3), 196−211.
(52) Nouasria, F. Z.; Selloum, D.; Henni, A.; Zerrouki, D.; Tingry, S. Gradient Doping of Cu(I) and Cu(II) in ZnO Nanorod Photoanode by Electrochemical Deposition for Enhanced Photocurrent Generation. *Ceram. Int.* **2021**, *47* (14), 19743−19751.
(53) Younas, M.; Shen, J.; He, M.; Lortz, R.; Azad, F.; Akhtar, M. J.; Maqsood, A.; Ling, F. C. C. Role of Multivalent Cu, Oxygen Vacancies and CuO Nanophase in the Ferromagnetic Properties of ZnO:Cu Thin Films. *RSC Adv.* **2015**, *5* (69), 55648−55657.
(54) Shaislamov, U.; Krishnamoorthy, K.; Kim, S. J.; Abidov, A.; Allabergenov, B.; Kim, S.; Choi, S.; Suresh, R.; Ahmed, W. M.; Lee, H.-J. Highly Stable Hierarchical p-CuO/ZnO Nanorod/Nanobranch Photoelectrode for Efficient Solar Energy Conversion. *Int. J. Hydrogen Energy* **2016**, *41* (4), 2253−2262.
(55) Liu, W. J.; Tang, X. D.; Tang, Z.; Bai, W.; Tang, N. Y. Oxygen Defects Mediated Magnetism of Ni-Doped ZnO. *Adv. Condens. Matter Phys.* **2013**, *2013*, No. 424398.
(56) Açıkgöz, M.; Drahus, M. D.; Ozarowski, A.; van Tol, J.; Weber, S.; Erdem, E. Local Coordination of Fe^{3+} in ZnO Nanoparticles: Multi-Frequency Electron Paramagnetic Resonance (EPR) and Newman Superposition Model Analysis. *J. Phys.: Condens. Matter* **2014**, *26* (15), No. 155803.
(57) Azamat, D. V.; Fanciulli, M. The Structure of Charge-Compensated Fe^{3+} Ions in ZnO. *Physica B* **2007**, *401*−*402*, 382−385.
(58) Yingsamphancharoen, T.; Nakarungsee, P.; Herng, T. S.; Ding, J.; Tang, I. M.; Thongmee, S. Ferromagnetic Behavior Due to Al^{3+} Doping into ZnO Nanorods. *J. Magn. Magn. Mater.* **2016**, *419*, 274−281.
(59) de Lara Andrade, J.; Oliveira, A. G.; Mariucci, V. V. G.; Bento, A. C.; Companhoni, M. V.; Nakamura, C. V.; Lima, S. M.; da Cunha Andrade, L. H.; Moraes, J. C. G.; Hechenleitner, A. A. W.; Pineda, E. A. G.; de Oliveira, D. M. F. Effects of Al^{3+} Concentration on the Optical, Structural, Photocatalytic and Cytotoxic Properties of Al-Doped ZnO. *J. Alloys Compd.* **2017**, *729*, 978−987.
(60) Ren, Q.; Cao, Y.-Q.; Arulraj, D.; Liu, C.; Wu, D.; Li, W.-M.; Li, A.-D. Review − Resistive -Type Hydrogen Sensors Hydrogen Sensors Based on Zinc Oxide Nanostructures. *J. Electrochem. Soc.* **2020**, *167* (6), No. 067528.
(61) Kavitha, R.; Kumar, S. G. A Review on Plasmonic Au−ZnO Heterojunction Photocatalysts: Preparation, Modifications and Related Charge Carrier Dynamics. *Mater. Sci. Semicond. Process.* **2019**, *93*, 59−91.
(62) Lupan, O.; Chow, L.; Chai, G. A Single ZnO Tetrapod-Based Sensor. *Sens. Actuators, B* **2009**, *141* (2), 511−517.
(63) Kohlmann, N.; Hansen, L.; Lupan, C.; Schürmann, U.; Reimers, A.; Schütt, F.; Adelung, R.; Kersten, H.; Kienle, L. Fabrication of ZnO Nanobrushes by H2−C2H2 Plasma Etching for H2 Sensing Applications. *ACS Appl. Mater. Interfaces* **2021**, *13* (51), 61758−61769.
(64) Zhang, Z.-Y.; Xiong, H.-M. Photoluminescent ZnO Nanoparticles and Their Biological Applications. *Materials* **2015**, *8* (6), 3101−3127.
(65) Chu, Y.-L.; Liu, Y.-H.; Chu, T.-T.; Young, S.-J. Improved UV Sensing of Au-Decorated ZnO Nanostructure MSM Photodetectors. *IEEE Sens. J.* **2022**, *22* (6), 5644−5650.
(66) Raji, R.; Gopchandran, K. G. Plasmonic Photocatalytic Activity of ZnO:Au Nanostructures: Tailoring the Plasmon Absorption and Interfacial Charge Transfer Mechanism. *J. Hazard. Mater.* **2019**, *368*, 345−357.
(67) Asadevi, H.; Kumari, P. P. N. C.; Amma, R. P.; Khadar, S. A.; Sasi, S. C.; Raghunandan, R. ZnO@MOF-5 as a Fluorescence "Turn-Off" Sensor for Ultrasensitive Detection as Well as Probing of Copper(II) Ions. *ACS Omega* **2022**, *7* (15), 13031−13041.
(68) Jankowska, D.; Muziol, T. M.; Mandal, D.; Kaczmarek-Kedziera, A.; Tepliakova, I.; Viter, R.; Barwiolek, M. M. ZnO−Benzimidazole Composite for Selective Detection of Zn2+ and Mg2+ Ions. *Spectrochim. Acta, Part A* **2025**, *343*, No. 126604.

https://doi.org/10.1021/acsanm.5c05081
ACS Appl. Nano Mater. 2026, 9, 3664−3678